Journal of Materials Chemistry A

Accepted Manuscript

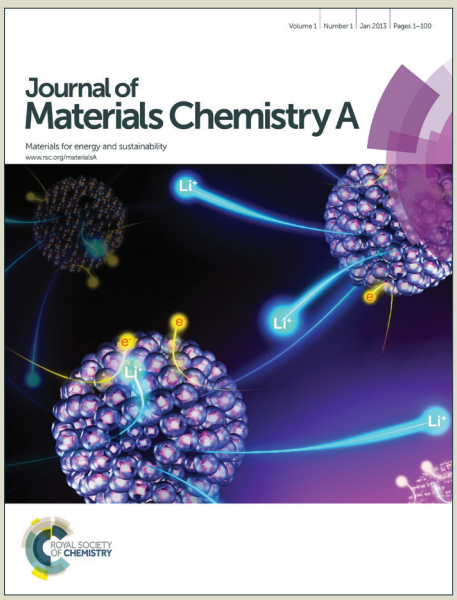

ROYAL SOCIETY OF CHEMISTRY

www.rsc.org/materialsA

Synthesis of ZnO@ZnS-Bi_2S_3 Core/Shell Nanorod Grown on Reduced Graphene Oxide sheets and Its Enhanced Photocatalytic Performance

Wang Xitao, Lv Rong, Wang Kang

Corresponding Author, Xitao Wang

Email: wangxt@tju.edu.cn

Address:

Collaborative Innovation Center of Chemical Science and Engineering (Tianjin),

Tianjin Key Laboratory of Applied Catalysis Science and Technology,

College of Chemical Engineering and Technology，

Tianjin University，Tianjin 300072，China

Telephone numbers: 86-022-27402972

Abstract

ZnO@ZnS-Bi_2S_3 core/shell nanorods anchored on reduced graphene oxide (RGO) were prepared by combining the hydrothermal treatment and ion exchange technique. The nanocomposites were characterized by scanning electron microscope (SEM), transmission electron microscope (TEM), X-ray diffraction, Raman, X-ray photoelectron spectroscopy (XPS), UV–Vis diffusion reflectance spectroscopy, room-temperature photoluminescence spectra (PL), and their photocatalytic performance for H_2 evolution under 300W Xenon lamp irradiation was evaluated. The as-prepared RGO/ZnO@ZnS-Bi_2S_3 core-shell nanorods display a wide and strong photo absorption in visible region and exhibit a higher photocatalytic activity for H_2 evolution from the glycerol water mixtures as compared with the RGO/ZnO nanorods and RGO/ZnO@ZnS core/shell nanorods. Under the optimal Bi_2S_3/ZnS molar ratio in the shell layer, the highest photocatalytic hydrogen production rate of 310 $\mu mol \bullet h^{-1}g^{-1}$ is observed. The highly improved performance of the composites can be ascribed to the increased light absorption and efficient charge separation.

Key words: reductive graphene oxide, ZnO@ZnS-Bi_2S_3 core/shell nanorods, Photocatalytic H_2 production, glycerol

1. Introduction

Photocatalytic hydrogen production by water splitting using solar energy has attracted a great research interest due to its advantages such as the abundant resource, low costs, and zero pollution. So far, numerous active photocatalysts such as various oxide, sulfide, and oxynitride semiconductors have been developed for the aforementioned photocatalytic reaction. Among them, ZnO is regarded as a good candidate for photocatalytic H_2 production because of its rapid generation of electron−hole pairs upon photo-excitation and highly negative reduction potential of excited electrons. Also, it shows the high activity for H_2 evolution under UV-light irradiation. However, its photocatalytic efficiency is limited and low because of its little energy utilization, small specific surface area for mass transfer, and the easy recombination of photoinduced electron-hole charge pairs, which are the most crucial obstacles limiting its further application. [1,2] To overcome these disadvantages and to achieve improved chemical and physical behaviours, many types of ZnO-based heterostructures for photocatalytic hydrogen production have emerged.[2-4] In these coupled semiconductors, ZnO-ZnS is a well-known photocatalyst. Theoretical calculations and experimental results have demonstrated that the combination of these two wide bandgap semiconductors can yield a novel material which has photoinduced threshold energy lower than that of the individual component. The conduction band of ZnS lies on a more negative potential than that of ZnO, whereas the valence band of ZnO is more positive than that of ZnS. [1-3] Thus, the band alignment can be achieved between ZnO and ZnS, which will be beneficial to improve the separation efficiency of photoinduced electrons and holes. Furthermore, the core/shell structured ZnO/ZnS nanorods have been demonstrated to possess improved physical and chemical properties for electronics, magnetism, optics, catalysis, and other applications. [5,6] Therefore, considerable efforts have been devoted to designing and controlling fabrication of core/shell structured ZnO/ZnS nanorods. To date, various preparation methods have been explored for the synthesis of ZnO/ZnS nanomaterial, and a number of morphologies have

been secured. [4,6,7] Although ZnO/ZnS core/shell nanorods display an improved photocatalytic performance for hydrogen production from water splitting as compared with the single phase ZnO or ZnS, the catalysis process is often found to be slow and inefficient for hydrogen production due to the weak absorption in the visible light region and the recombination of photo-generated electron and hole. This means that the photo absorption and the charge transfer rate of ZnO/ZnS core/shell nanorods involved in the process needs to be improved.

A considerable enhancement in the photocatalytic efficiency of wide bandgap semiconductor under visible light has been obtained by coupling low bandgap semiconductor including CdSe, CdS, Cu_2O, and Fe_2O_3. With coupling nanoscale low-bandgap semiconductor, it can be expected that the photocatalytic activity of ZnO@ZnS core/shell nanorods will be significantly improved by the enhancement of charge separation and photo absorption even under visible light. [8-10] As an important chalcogenide compound, Bi_2S_3 has been used in optical and electronic devices such as photovoltaic cells, photoconductors, infrared (IR) detectors, and superionic conductors. [11,12] In particular, the low bandgap energy (about 1.36 eV) of Bi_2S_3 increases the capability of absorbing a broad solar spectrum, which makes Bi_2S_3 an effective semiconductor material for photocatalytic application.[13]

In addition, a variety of attempts have been tried to combine active photocatalytic semiconductors with graphene oxide (GO) or reduced graphene oxide (RGO) to improve the photocatalytic activity [14-19]. For example, Pan et al. [14] have successfully fabricated ZnO–reduced graphene oxide (RGO) composites via UV-assisted photocatalytic reduction of GO by ZnO nanoparticles and the ZnO–RGO composites exhibit an enhanced photocatalytic performance in reduction of Cr(VI) under UV light irradiation as compared with pure ZnO. Xu et al. [15]report the synthesis of RGO/ZnO composites with different particle size of ZnO via a facile solvothermal approach and investigate the photocatalytic activity and stability of RGO/ZnO composites toward degradation of organic dyes and reduction of Cr(VI) in an

aqueous phase. Vietmeyer et al. [16] have established an excited state interaction between functionalized carbon nanotube (CNT) and ZnO, ZnO-reduced graphene oxide (RGO) hybrid might be a suitable choice for dye degradation. Lv and co-workers [17] have developed ZnO-RGO hybrid composites by using a microwave synthesis system, resulting in improved degradation of methylene blue. The recent studies have revealed that the enhanced photocatalytic efficiency of these composites mainly contribute to the increasing adsorptivity of reactant, extended light absorption range, and especially efficient charge transportation and separation [17-19]

The hexagonal atomic structure of graphene might be able to supply a building platform for the epitaxial growth of other hexagonal nanostructure such as ZnO.[20] Several researches have reported that well aligned ZnO nanorods anchored vertically on RGO sheets can accelerate the charge transportation and separation, and remarkably improve light absorption in visible range and photocatalytic efficiency over these nanocomposites. Meanwhile, the introduction of ZnS-Bi_2S_3 bi-component shell onto the ZnO nanorods will have significant influence on the photo absorption, separation and transfer of photo-generated carriers and photocatalytic activity of RGO/ZnO nanorods composites. However, to our best knowledge, the synthesis and application of the structure of ZnO@ZnS-Bi_2S_3 core/shell nanorods grown on RGO sheets have not reported.

Therefore, in present work the successful fabrication of ZnO@ZnS-Bi_2S_3 core/shell nanorods anchored on RGO sheets via combining a hydrothermal growth, liquid-phase chemical conversion and ion exchange was reported. We demonstrated the pioneer work of employing the ZnO@ZnS-Bi_2S_3 core/shell nanorods anchored on RGO sheets in hydrogen production from a glycerol aqueous solution under 300W Xe lamp irradiation in a tank reactor. The effects of Bi_2S_3/ZnS molar ratios on the morphology, photo absorption and the activity of RGO/ZnO@ZnS- Bi_2S_3 nanorods will be elucidated in detail.

2. Experimental

2.1 Preparation of nanocomposites

All reagents used in the experiment were of analytical grade and used without any further purification.

2.1.1 Preparation of ZnO nanorods grown on RGO sheets

20mL GO solution (2mg/mL) prepared by the simplified Hummers method was mixed with 25 mL ethanol solution of $Zn(CH_3COO)_2$ (0.05 mol•L^{-1}). The solvent of mixture was gradually evaporated in a water bath at 80^{o}C under mild magnetic stirring. The sample was calcined at 400 ^{o}C for 1 h in N_2 atmosphere to obtain ZnO seed layer on RGO sheets.

The as-prepared ZnO seed layer was added into 25mL aqueous solution of PVP (4mg/mL), and dispersed under ultrasonication for 3h. After that, it was cooled in an ice bath while an solution of 0.4g $Zn(NO_3)_2$•$6H_2O$ dissolved in 25mL water was added drop by drop with pH of ~14 which was adjusted by 5 mol•L^{-1} NaOH solution. Subsequently, the solution was stirred at 60 ^{o}C for 5 h. After reaction, the resultant sample was subjected to hydrothermal treatment in a Teflon bottle at 180 ^{o}C for 36 h. Finally, the product was washed with deionized water and ethanol, and then dried at 80 °C.

2.1.3 Synthesis of ZnO@ZnS core/shell nanorods grown on RGO sheets

0.045 g Na_2S was dissolved in 70 ml deionized water. 0.1 g as-prepared ZnO nanorods/RGO was well dispersed in the above sodium sulfide solution under stirring, and then the suspension was placed in a 70 °C water bath with magnetic stirring for 5 h. The production is collected by centrifugation of the aforementioned suspension with washing of deionized water, and dried at 80 °C for 12 h. Thereafter, the ZnO/ZnS core/shell nanorods with a ZnS/ZnO molar ratio of about 0.1 were prepared (The amount of ZnS on the surface of the ZnO nanorods was calculated based on the S^{2-} moles consumed in the reaction.).

2.1.3 Synthesis of ZnO@ZnS-Bi_2S_3 core/shell nanorods grown on RGO sheets

The RGO/ZnO@ZnS-Bi_2S_3 core/shell composite were prepared by the chemical conversion process using ZnS on the shell of ZnO/ZnS nanorods as sacrificial template to Bi_2S_3. In a typical synthesis, 0.1 g the as-prepared RGO/ZnO@ZnS were dispersed into 100 ml deionized water under magnetic stirring, and then a solution of a certain amount of $Bi(NO_3)_3$ dissolved in 50 mL glycerol aqueous solution(25 wt.%) was added. After treating at 90°C for

30 min, the final products were collected by centrifugation, washed thoroughly using deionized water to remove any coprecipitated salts, and then dried in a vacuum oven at 80°C overnight. By varying the concentration of $Bi(NO_3)_3$ solution, three ZnO/ZnS-Bi_2S_3 nanorods anchored on RGO sheets with different Bi_2S_3/ZnS molar ratios(0.15, 0.3 and 0.45) were obtained, marked as RGO/ZnO@ZBS-X (X=1, 2, 3), respectively.

For comparison, ZnO@ZBS-2 core/shell nanorods without RGO were also prepared by the method above.

2.2 Characterization

The morphology of the RGO/ZnO composites was characterized by a Hitachi S-4800 scanning electron microscope (SEM, 5 kV). Transmission electron microscopy (TEM) and higher-magnification transmission electron microscopy (HRTEM) were obtained with JEOL-2100F system (200 kV). Specimens for TEM and HRTEM measurements were prepared via drop-casting a droplet of ethanol suspension onto a copper grid, coated with a thin layer of amorphous carbon film, and dried in air.

X-ray diffractometer (XRD) of the samples were recorded on a D/MAX-2500 automatic powder diffractmeter equipped with the graphite monochromatized Cu Kα radiation flux (λ = 0.15418 nm) at a scanning rate of 0.02 s^{-1} in the 2θ range of 20-90°.

X-ray photoelectron spectroscopy (XPS) measurements were recorded with an SSX-100/206 probe using nonmonochromatized Al-Mg Ka X-ray as the excitation source (Japan). Binding energy was calibrated with respected to the signal for C 1s of 284.8 eV.

The Fourier transform infrared (FT-IR) spectra are recorded with Thermo Nicolet Nexus using the KBr disk method.

Raman spectra were recorded from 0 to 3500 cm^{-1}on a DXR Raman microscope (Thermo Scientific, American) using a 532 nm high brightness laser excitation.

Ultraviolet and visible diffusive reflectance spectra (UV–Vis DRS) were taken on an UV–Vis spectrometer (Perkin Elmer, Lambda 750), the scanned range being 200–800 nm against barium sulfate standard.

Room-temperature photoluminescence spectra (PL) were executed on powder samples by using a Fluorolog3 photoluminescence spectrometer (Horiba Jobin Yvon, Japan). The excitation wavelength was 325 nm, and the spectra were recorded in the range of 360-650 nm.

2.4 Photocatalytic activity test

The photocatalytic performance of the samples was evaluated by H_2 production from a glycerol/water mixed solution under a 300W Xenon lamp (PLS-SXE300C, Beijing Perfectlight Co., Ltd., wavelength range:300-2500 nm) in a tank reactor equipped with a top quartz glass with diameter of 5cm as shown in Fig.1. In a typical experiment, 50 mg of photocatalyst was suspended in 230 mL of 5% glycerol ($C_3H_8O_3$) solution under magnetic stirring. The temperature of the solution was maintained at room temperature by a flow of cooling water. Prior to the irradiation, the photocatalytic reaction system was flushed with an Argon flow of 30 mL/min for 2h to remove the air in the reactor, then an Argon flow of 10 mL/min was used as a carrier gas through the reactor to the analysis system. The products of the reaction were analyzed by an on-line gas chromatography using thermal conductivity detector (Agilent 4890, nitrogen as a carrier gas).

The hydrogen production rate is calculated as following formula.

$$\text{Hydrogen production rate } (\mu\text{mol} \cdot \text{h}^{-1} \cdot \text{g}^{-1}) = \frac{\text{H}_2\%(^{\text{V}}/_{\text{V}}) * \text{Flowrate}(600\text{ml/h})}{22414(\text{ml/mol})} * 10^6 * (1000\text{mg}/50\text{mg})$$

3 Results and discussion

3.1. Morphology and structure of nanocomposites

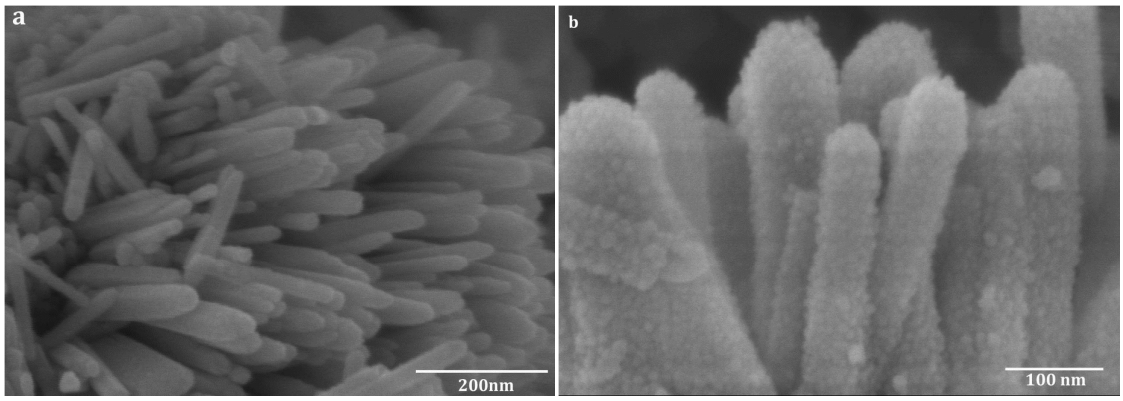

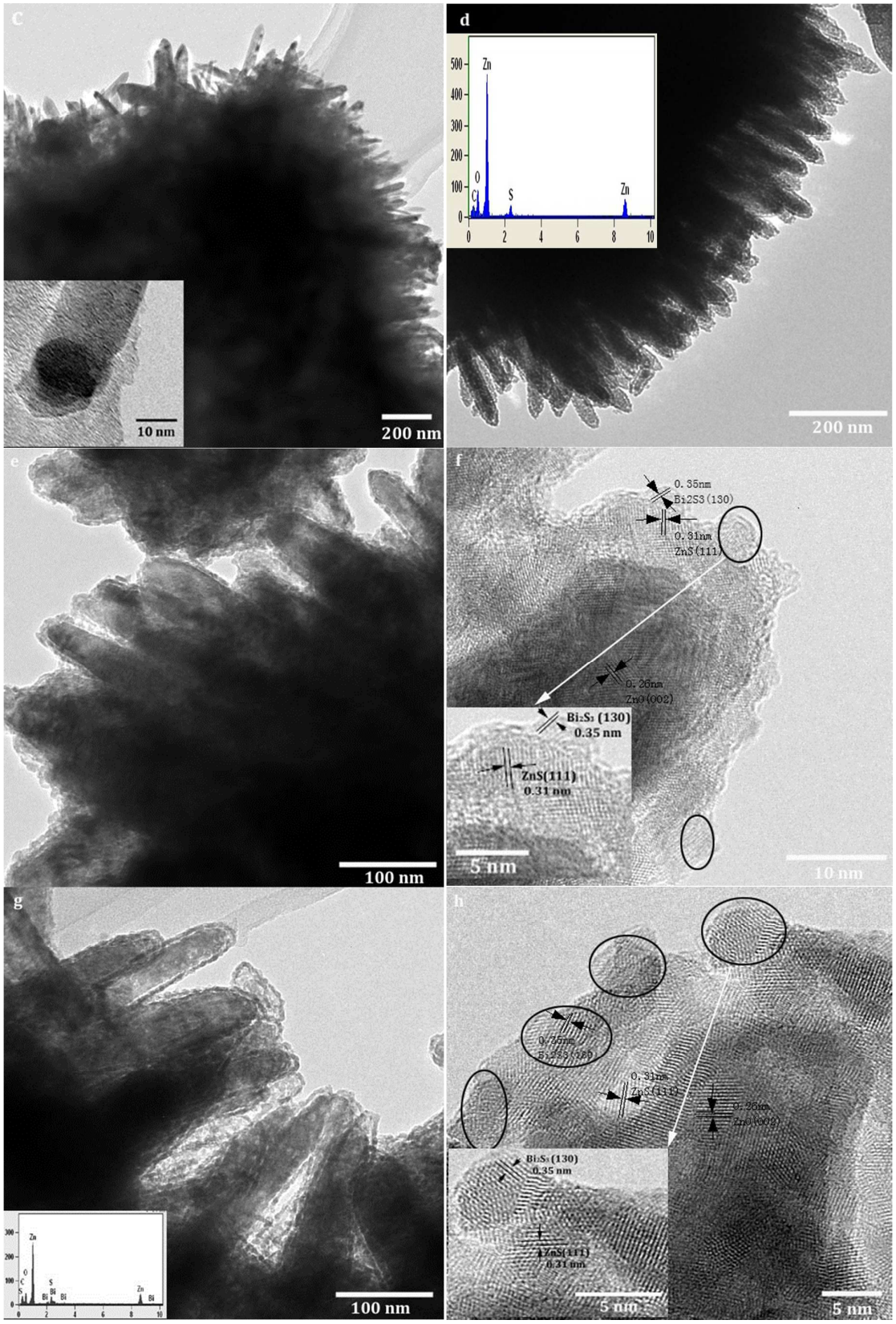

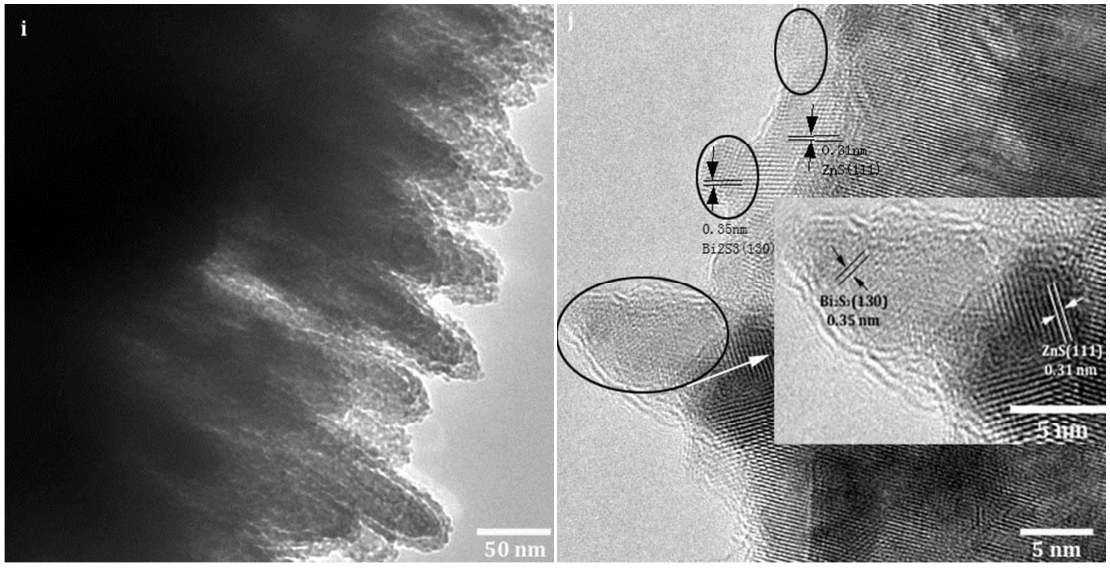

Fig.1 The SEM and TEM images of (a, c)RGO/ZnO, (b, d) RGO/ZnO@ZnS; TEM and HRTEM images of (e, f)RGO/ZnO@ZBS-1,v(g, h)RGO/ZnO@ZBS-2, (i, j)RGO/ZnO@ZBS-3

The SEM, TEM and HR-TEM images of ZnO nanorods, ZnO/ZnS core/shell nanorods and ZnO/ZnS-Bi_2S_3 core/shell nanorods anchored on RGO sheets are displayed in Fig. 1. It can be clearly seen from SEM and TEM images of RGO/ZnO nanorods (Fig. 1(a) and (c)) that the structure of ZnO nanorods grown on RGO sheets was formed. The uniform nanorods with estimated length of 200~300 nm and diameter of 50~60 nm were anchored on the entire RGO sheet. The direct growth of ZnO nanorods on RGO sheets can be confirmed from the inset in Fig.1(c). After the deposition of ZnS, the surface of the ZnO nanorods became rougher and thicker, indicating the conversion of ZnO to ZnO/ZnS core/shell structure via the surface sulfidation. The chemical composition of graphene/ZnO was analyzed by an energy dispersive spectrometer (EDS) spectrum on an SEM (the inset in Fig. 1(d)). The result shows the peaks of C, O, Zn and S, confirming the formation of ZnS shell.

When RGO/ZnO@ZnS composites were added into $Bi(NO_3)_3$ solution, cation exchange began at the interfaces between the ZnS shell layer surfaces and $Bi(NO_3)_3$ solution. With the increase in the concentration of $Bi(NO_3)_3$, ZnS was gradually substituted by Bi_2S_3, resulting in an Bi_2S_3-ZnS bi-component shell layer. The conversion dynamic of single component shell

to bi-component shell comes from the marked difference in solubility-product constant (Ksp) between ZnS (Ksp= 2.93×10^{-25}) and Bi_2S_3 (Ksp = 1.0×10^{-97}). [21] The TEM images in Fig. 1(e), (g) and (i) show the structure of ZnO/ZnS-Bi_2S_3 core/shell nanorods anchored on RGO sheets. The HRTEM images taken from the edge of rods in Fig. 1(f), (h) and (j) show that the shell is composed of tiny primary particles around 3-5 nm in diameter and the thickness of ZnS-Bi_2S_3 shell is about 5-8nm. Also, HRTEM images further reveal structural information of the ZnS-Bi_2S_3 shell. The interplanar spacing of 0.31nm corresponding to the (111) interplanar spacing of the standard zinc blend ZnS, and 0.35nm owing to the (130) interplanar spacing of Bi_2S_3 can be observed, which confirms the transformation of ZnS to Bi_2S_3. With the increase of $Bi(NO_3)_3$ concentration, the amount of Bi_2S_3 particles increase gradually. The EDS spectrum of RGO/ZnO@ZBS-2 nanorods shown in the inset of Fig. 1(i) indicates that the as-prepared composites are composed of Zn, Bi, S, O and C elements, which confirms the successful incorporation of Bi element into the ZnS shell after the cation exchange. Moreover, these images also confirm that the shell boundary between ZnS and Bi_2S_3 is free of amorphous phases, which is an indication of the formation of atomic hetero-junctions. The intimate lattice contact between the ZnS and Bi_2S_3 would be in favor of efficient photo-generated electrons and holes transfer across the ZnS-Bi_2S_3 interface and consequently reduce the recombination of photo-generated carriers. This reasoning is also supported by literature [13].

The crystal quality and orientation of the as-synthesized nanocomposites were analyzed by X-ray diffraction (XRD) as shown in Fig. 2(A). All patterns of nanocomposites exhibit sharp peaks, indicating that all samples were highly crystalline. The diffraction peaks of the curve a can be assigned to hexagonal ZnO (JCPDS36-1451), and no impurity peaks are observed. The patterns of the ZnO/ZnS core/shell nanorods (curve b) consist of two sets of diffraction peaks (ZnO and ZnS), and the broadening peak at $2\theta=28.62°$ match well with the face-centred-cubic

ZnS (JCPDS65-0309). Because the peaks at 2θ=47.83° of (220) and 2θ=56.76° of (311) crystal plane are very close to the diffraction peaks of (102) and (101) crystal plane of ZnO, these peaks are overlapped together, respectively. The intensity of the ZnO diffraction peaks decrease obviously with the formation of ZnS shell layer on the ZnO nanorods. After the conversion of ZnS to Bi_2S_3, peaks corresponding to ZnS become weaker gradually and almost disappear following the increase of concentration of $Bi(NO_3)_2$ solution. The diffraction peak corresponding to Bi_2S_3 cannot be observed due to the highly distribution and small size of Bi_2S_3 particles.

Absence of the (002) diffraction line of GO at around 10° and RGO at 24° in the XRD patterns of all nanocomposites indicates a complete reduction of GO by solvothermal process during the growth of ZnO and the disorder of layer spacing due to the growth of ZnO nanorods between the adjacent graphene sheets as reported in reference 22 and 23. Thus, the formation of nanocomposites between ZnO@ZnS-Bi_2S_3 core/shell nanorods and RGO is confirmed from the XRD results.

FT-IR spectroscopy was used to identify the reduction of oxygen-containing groups of GO and chemical interaction between ZnO nanorods and RGO. Fig. 2(B) shows the FT-IR spectra of RGO/ZnO nanorod composite and its residual graphene after dissolving in solution of hydrochloric acid. For ZnO nanorod/RGO composite, the absorption bands at 3442 cm^{-1} (O-H stretching vibration)[28], 1642 cm^{-1} (O-H bending vibration)[28], 1565 cm^{-1} (the skeletal vibration of the graphene sheets) [14,28] , 1393 cm^{-1}(tertiary C-OH groups)[29] and 892 cm^{-1} (C-C bending vibration)[29] were observed. The FT-IR spectrum of nanocomposites and residual graphene confirmed the reduction of GO sheets because the absorption due to the C=O group at 1726 cm^{-1} was absent, and O-H (carboxyl) groups at 1393 cm^{-1} was very weak. The absorption band at 411 cm^{-1} is detected in the FT-IR spectrum, which is due to the formation of Zn-O bond. When compared to the FT-IR spectra of residual graphene, it can be seen that the peaks corresponding to the reduced graphene oxide at 1565 cm^{-1} and 892 cm^{-1} in ZnO nanorod/RGO composite become stronger, indicating the strong chemical interaction between ZnO nanorods and RGO sheets. In addition, a new absorption band appears at 1216 cm^{-1} after the growing of the ZnO nanorods on RGO sheets, whereas it cannot be observed in residual graphene. This result suggests that this band is derived from the chemical interaction of RGO

and ZnO. Therefore, we can conclude that the absorption band at 1229 cm^{-1} is ascribed to the C-O-Zn linkage.

To further confirm the composition of sample and conversion of ZnS into Bi_2S_3, Raman spectrum of RGO/ZnO@ZBS-2 composite was recorded as shown in Fig.2 (C). The Raman spectrum of RGO/ZnO@ZBS-2 exhibits two vibrations at around 1589 cm^{-1} and 1347 cm^{-1} related to the D band and G band of RGO, indicating the presence of RGO. In addition, five distinct Raman peaks at 558.8, 428.8, 322.9, 192.8 and 96.5 cm^{-1} are observed. The peaks located at 558.8cm^{-1} and 433.7cm^{-1} are ascribed to the A_1(LO) modes and E_2 (high) phonons of ZnO nanorods[24], respectively. The band at 322.9 cm^{-1} corresponds to the surface optic (SO) phonon scattering of ZnS nanoparticles [25]. The peaks at 192.8 cm^{-1} and 96.5 cm^{-1} can be attributed to Bi_2S_3, which agree with two Raman bands reported by Loh et al. [26]and Cao et al. [27] This result reveals that nanocomposite is composed of ZnO, ZnS, Bi_2S_3 and RGO. Also, it can be regarded as the direct evidence for the formation of Bi_2S_3 on the shell.

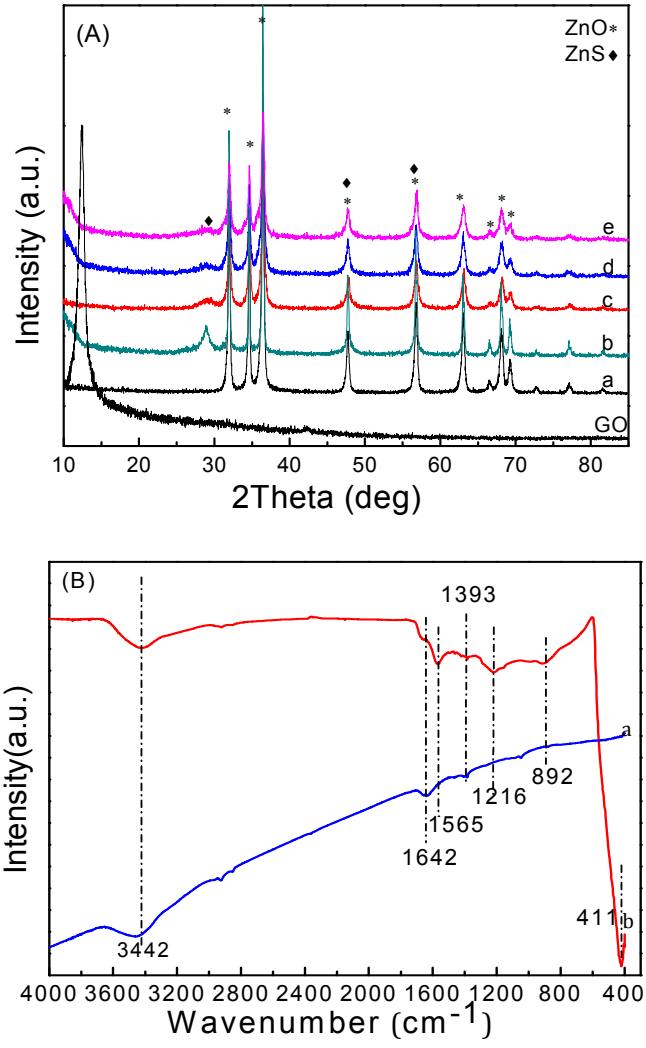

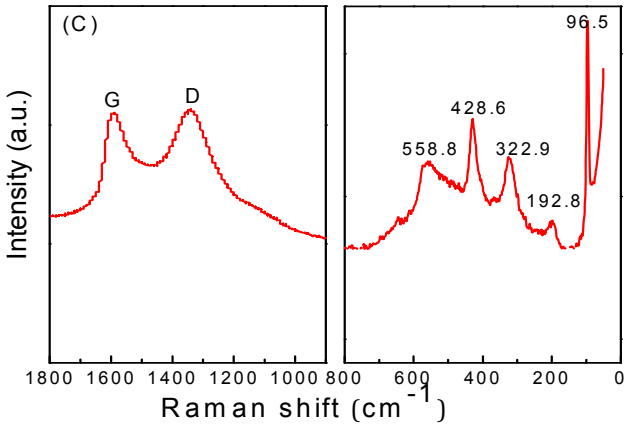

Fig. 2 (A) XRD patterns of (a)RGO/ZnO, (b)RGO/ZnO@ZnS, (c)RGO/ZnO@ZBS-1, (d) RGO/ZnO@ZBS-2, (e) RGO/ZnO@ZBS-3; (B) FT-IR spectra of the residual graphene after dissolving ZnO nanorods/RGO in a solution of hydrochloric acid (a) and ZnO nanorods/RGO (b); (C) Raman spectra of RGO/ZnO@ZBS-2

Further evidence for the composition of the ZnO@ZnS-Bi_2S_3/GO composites was obtained by the X-ray photoelectron spectra (XPS, Fig. 3). The survey spectrum shows the presence of Zn, Bi, S and O as well as C. The higher-resolution spectrum of C1s XPS spectrum for composites indicates a considerable degree of graphene oxide with three main components that correspond to carbon atoms in different functional groups: the non-oxygenated C-C bond (284.61 eV), the C-O of epoxy and hydroxyl (286.65 eV), and the carbonyl C=O (288.85 eV) [22,23]. The concentration of the oxygen–containing bonds (C-OH, C-O and O=C-OH) were very low, which indicated an effective chemical reduction of the graphene oxide platelets to graphene ones in nanocomposites. The predominant O1s peak of the all samples can be separated into two components at around 531.6 eV and 530.1 eV, which can be related to the crystal lattice O^{2-} in ZnO and the chemisorbed oxygen caused by surface hydroxyl, respectively [30]. When compared to RGO-ZnO nanocomposites, the O1s peaks of RGO/ZnO@ZnS and RGO/ZnO@ZBS-2 corresponding to the crystal lattice O^{2-} in ZnO and OH group shifted gradually to a higher energy. This shift could be ascribed to the strong interaction between ZnS and ZnO.[31]

The positions of the S*2p* and Zn*2p* signals for the ZnO@ZnS core/shell nanorods-RGO sample are around 161.7 and 1021.4eV (not shown) which is similar to the value of the Zn-S bond in the literature [33]. This finding indicates that the corresponding deposition shell layer is ZnS. As for the RGO/ZnO-ZBS-2 sample, peaks at 158.7, 161.6, 162.7 and 164.0 eV due to

$Bi4f_{7/2}$, $S2p_{3/2}$, $S2p_{1/2}$ and $Bi4f_{5/2}$ can be detected, which demonstrates that the main chemical state of Bi in the samples was +3, and that of S was -2.[32,33] These results illustrate the formation to ZnS-Bi_2S_3 bi-component shell in RGO/ZnO@ZBS compostites.

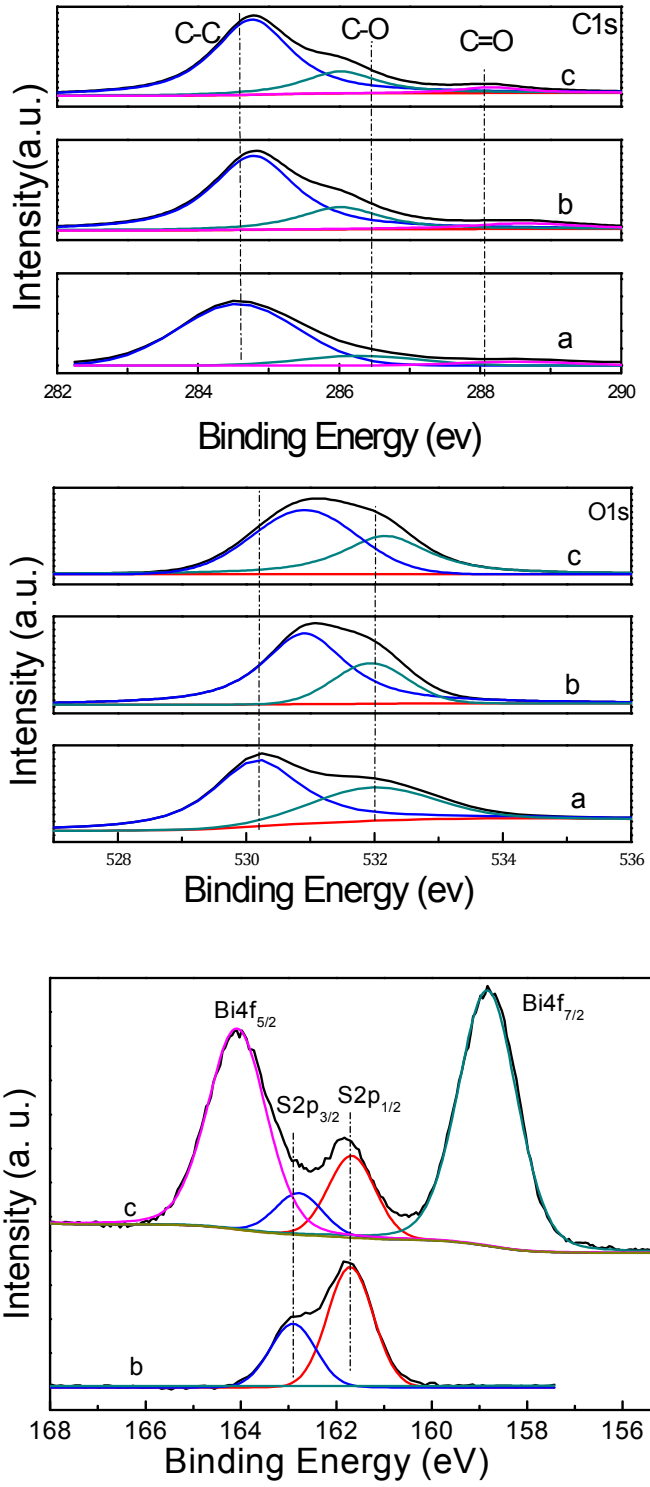

Fig.3 the X-ray photoelectron spectra of (a) RGO/ZnO; (b)RGO/ZnO@ZnS; (c)RGO/ZnO@ZBS-2

3.3 optic properties of RGO/ZnO@ZnS-Bi_2S_3 composites

Photoluminescence (PL) spectroscopy is a facile technique to survey the separation efficiency of the photo-generated charge carriers, for it mainly results from the recombination of free carriers. Fig. 4(A) shows the PL spectra of the RGO/ZnO@ZnS-Bi_2S_3 with different Bi_2S_3/ZnS molar ratios compared with that of bare ZnO and RGO/ZnO nanorods. As can be seen from Fig. 4 (A), the bare ZnO nanorods display strong fluorescence emission at the range of 370-390 nm and 400 to 540 nm. The peak at the range of 370-390 nm can be ascribed to excitation recombination [34,35], which occurs due to recombination between the electrons in conduction band and the holes in a valence band. While, the blue and green emissions at the range of 400 nm to 540 nm are generally believed coming from the surface defects of ZnO. It is evident that the fluorescence emission intensity of ZnO/RGO nanocomposites decreases dramatically when compared to that of pure ZnO nanorods. This phenomenon suggests that the RGO/ZnO nanocomposites have a lower recombination rate of electrons and holes, which is the fact that the electrons are excited from the valence band of ZnO nanorods to the conduction band and then transfer to RGO sheets, preventing a direct recombination of electrons and holes. After the introduction of ZnS and ZnS-Bi_2S_3 shell, fluorescence emission at the range of 370-390 nm decreases slightly, whereas the blue and green emissions at the range of 400 nm to 540 nm significantly decreases, implying that the recombination of photo-generated carriers was effectively suppressed due to the composite effect of semiconductors. It is notable that the emission intensity of RGO/ZnO@ZBS decreases first with the increase of Bi_2S_3/ZnS molar ratio, then increase with the further increase of that, which indicates that there is an optimum molar ration of Bi_2S_3/ZnS for suppressing the recombination of photo-generated carriers. The higher recombination rate of electrons and holes over RGO/ZnO@ZBS-3 nanocomposites can be due to the formation of larger particles and thicker layer of Bi_2S_3 when the Bi_2S_3 content is increased, in which photo-generated hole and electrons would more easily recombine.

Moreover, it can be found that the RGO has a significant influence on the separation of photogenerated carriers when compared the PL spectrum of RGO/ZnO@ZBS-2 to that of ZnO@ZBS-2. This result illustrates that RGO materials are relatively good electron acceptors; the synergistic effect between RGO and semiconductor components would effectively reduce recombination and lead to an increased charge carrier separation.

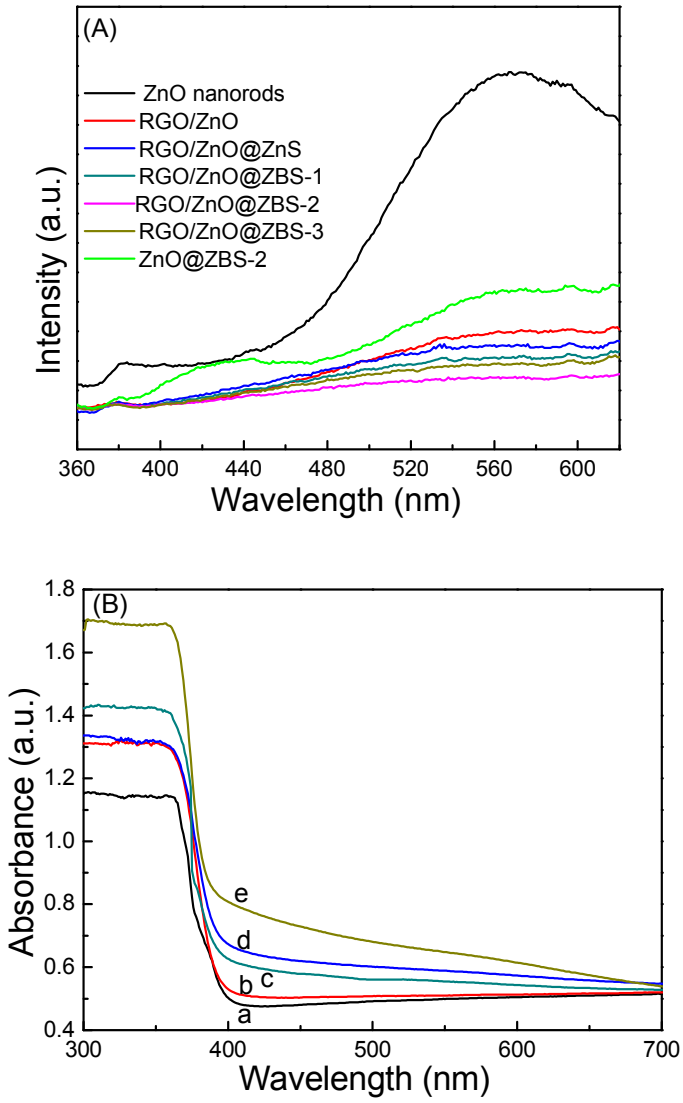

Fig.4 (A) Room-temperature PL spectra of (a)ZnO nanorods, (b)RGO/ZnO, (c)RGO/ZnO@ZnS, (d)RGO/ZnO@ZBS-1,(e) RGO/ZnO@ZBS-2, (f) RGO/ZnO@ZBS-3, (g)ZnO@ZBS; (B) UV–Vis DRS of (a) RGO/ZnO, (b)RGO/ZnO@ZnS, (c)RGO/ZnO@ZBS-1, (d)RGO/ZnO@ZBS-2, (e)RGO/ZnO@ZBS-3

The UV–vis absorption spectra of the as-synthesized RGO/ZnO@ZnS-Bi_2S_3 nanocomposites with different Bi_2S_3/ZnS molar ratios, together with RGO/ZnO and RGO/ZnO@ZnS for comparison are shown in Fig.4(B). The strong characteristic absorption peak at around 384 nm for all samples indicates the existence of highly crystalline ZnO. [2] RGO/ZnO@ZnS and RGO/ZnO composites exhibit the similar spectra, which possesses strong UV light absorption and weak visible light absorption. This can be due to the wide

bands of two samples. After the conversion of ZnS to Bi_2S_3 on the shell, the nanocomposites showed good absorption in the visible region (λ= 400-700 nm) as well as in the UV region, suggesting that these samples might exhibit good photocatalytic behaviors under visible light. It can be observed clearly that the upper branch of the spectra at the wavelength of less than 400 nm practically coincides with the UV–Vis DRS spectrum of RGO/ZnO@ZnS, whereas the broad absorption in the visible region is caused by the Bi_2S_3 coupling effect. The broadened peaks in the wavelength range 500-800 nm are similar to the characteristic absorption spectra of Bi_2S_3 reported elsewhere.[13,36] Moreover, the absorption of the RGO/ZnO@ZnS-Bi_2S_3 samples in the visible region become stronger with increasing of the Bi_2S_3/ZnS molar ratio, indicating the increase of Bi_2S_3 content.

3.4 Photocatalytic activity

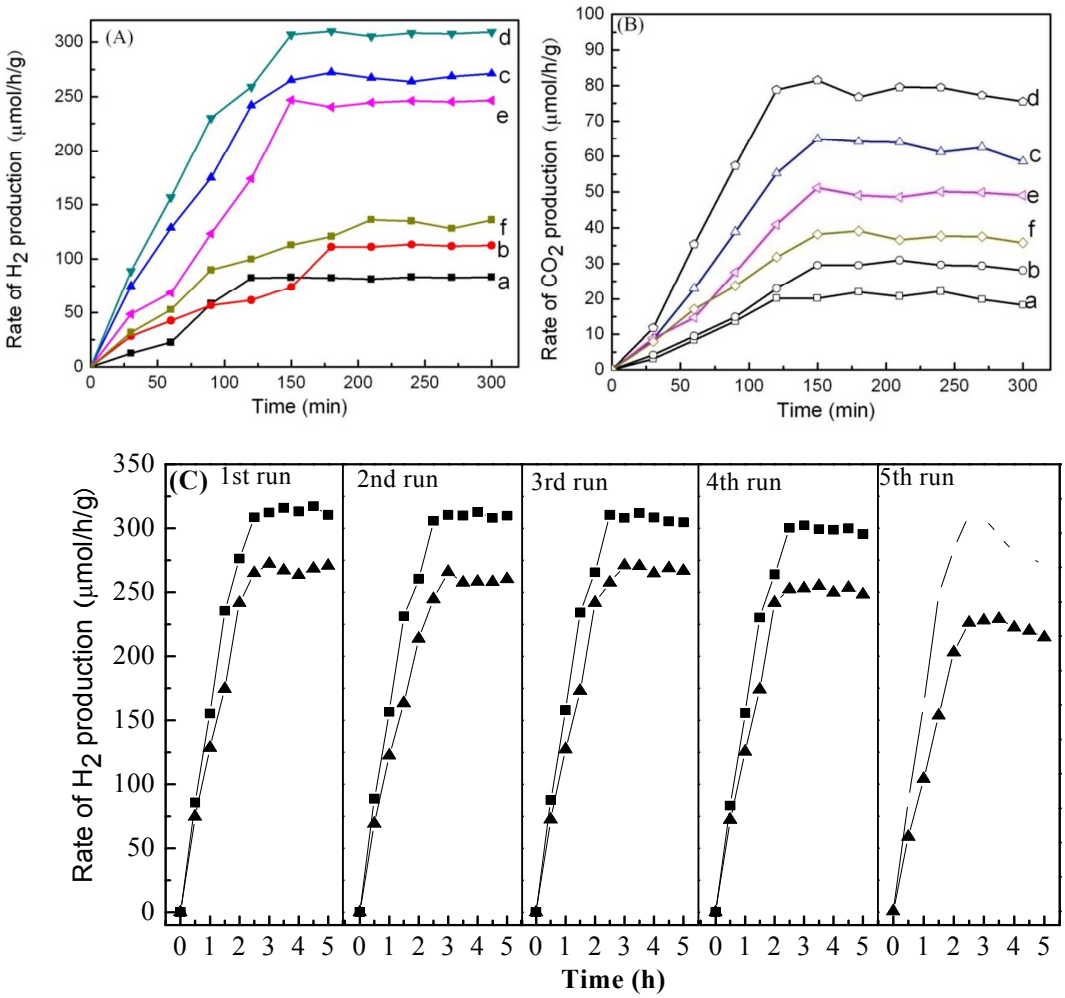

Fig. 5 (A) Rates of the photocatalytic H_2 production and (B) Rates of the photocatalytic CO_2 production from glycerol solution (5%) under the irradiation of 300W Xe lamp over

nanocomposites:(a)RGO/ZnO, (b)RGO/ZnO@ZnS, (c)RGO/ZnO@ZBS-1, (d)RGO/ZnO@ZBS-2, (e)RGO/ZnO@ZBS-3, (f)ZnO@ZBS-2; (C) Rates of the photocatalytic H_2 production in cycles over RGO/ZnO@ZBS-1(▲) and RGO/ZnO@ZBS-2(■)

The photocatalytic performances of all nanocomposites were evaluated by the rates of the photocatalytic H_2 production from glycerol solution (5%) under Xenon lamp (300W) irradiation. Typical results obtained are shown in Fig. 5(A), where the rates of hydrogen production are plotted as functions of irradiation time. It is observed that the rates of hydrogen production for all catalysts increase firstly with reaction time and reach the plateau at ca. 120 min. The activity of the RGO/ZnO nanorods under Xe lamp irradiation is quite low ($82 \mu mol \bullet h^{-1} \bullet g^{-1}$). After the deposition of the ZnS nanoparticles on the surface of the ZnO nanorods, the hydrogen yields are improved slightly. Fig. 5(A) also shows that the effects of Bi_2S_3 content on the photocatalytic activity of the RGO/ZnO@ZnS nanorods. All Bi_2S_3 containing composite nanorods display a photocatalytic H_2 evolution rate much higher than that of RGO/ZnO@ZnS, revealing that the Bi_2S_3 in the shell affects greatly the photocatalytic activity of RGO/ZnO@ZnS nanorods. The rate of the photocatalytic H_2 production initially increases with an increase of Bi_2S_3 content in the shell, and then it decreases with the further increase of Bi_2S_3 amount. The RGO/ZnO@ZBS-2 nanorods exhibit a maximum H_2 production rate of 310 $\mu mol \bullet h^{-1} \bullet g^{-1}$, about 3.8 and 2.9 times more active than RGO/ZnO and RGO/ZnO@ZnS samples, which is comparable to that over Pt/TiO_2 photocatalyst as reported. [37] Production of H_2 is accompanied by evolution of CO_2, the rate of which goes through a maximum after ca. 150 min and then remains almost unchanged during the reaction [Fig 5(B)]. The CO_2 evolution amounts over these samples follow similar trend with H_2. For all composites, the H_2/CO_2 molar ratio is much higher than 2.33, the theoretical value calculated for the total mineralization of glycerol [Eq.(1)]. This result suggests that the presence of by-products in solution results from the partial dehydrogenation/oxidation of glycerol. Previous studies [37–40] clearly show that water acts as an oxidizing agent, via intermediate formation of

hydroxyl radicals and other photo-generated oxidants, and that the photo-catalytic process occurs via oxidation of the glycerol toward molecules of progressively lower molecular weight and, eventually, CO_2. The formation of lower molecular weight intermediates must decrease the production of CO_2. In addition, organic intermediates could not be observed due to their low concentrations in glycerol solution after a short reaction time.

$$C_3H_8O_3 + H_2O \xrightarrow{hv} 3CO_2 + 7H_2 \quad (1)$$

According to the discussion on characterizations mentioned above, RGO/ZnO@ZBS-2 nanorods with a proper Bi_2S_3/ZnS molar ratio and thickness of Bi_2S_3 layer in the shell has higher synergistic effect between ZnS and Bi_2S_3 compared to the other two samples, which favours the separation and transfer of photoinduced charge carriers, finally inhibiting the recombination of charge carriers. The decrease in photocatalytic performance of the RGO/ZnO@ZBS-3 sample can be attributed to the agglomeration of Bi_2S_3 into larger particles and thicker Bi_2S_3 layer in the shell, which in turn results in an increase in recombination rate of photo-generated electrons and holes. In addition, ZnO@ZBS-2 exhibits inferior photocatalytic activity when compared to RGO/ZnO@ZnS-Bi_2S_3 samples; this may be due to the higher recombination rate of photo-generated electron and hole as revealed by PL analysis. Thus, the existence of RGO is a key factor for enhanced photocatalytic performance.

The stability of RGO/ZnO@ZBS-1 and RGO/ZnO@ZBS-2 photocatalyst was confirmed experimentally by recycling this sample [Fig. 5(C)]. Consequently, the high activity for the photocatalytic H_2 production from glycerol solution can be maintained nearly unchanged after four cycles, and still more than 80% even after five cycles. The results indicate that the photocatalysts are highly efficient and stable under the irradiation of 300W Xe lamp. In order to investigate the reason for the decrease in H_2 production rate after 20 h reaction, the XPS of fresh and spent RGO/ZnO@ZBS-1were performed. It can be seen from Fig. 6 that for spent

RGO/ZnO@ZBS-1sample, two new XPS peaks related to Bi $4f_{7/2}$ and Bi $4f_{5/2}$ appear at 163.4 eV and 158.2 eV as compared to the fresh one, which are much higher than reported value for elemental Bi [41] and lower than those reported for Bi in Bi_2S_3 [32,33], indicating the formation of a small part of Bi^{2+}. This can be due to the photo-reduction of Bi^{3+} in the reaction $Bi^{3+} + e \rightarrow Bi^{2+}$, which will result in the deactivation of photocatalyst.

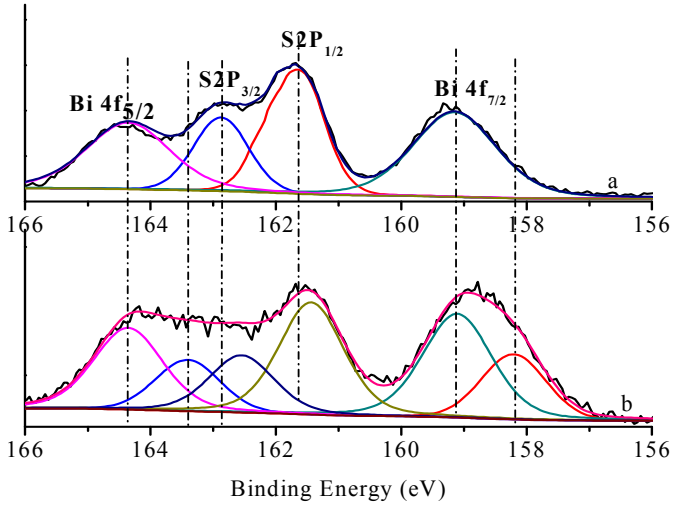

Fig.6 the X-ray photoelectron spectra of (a) fresh RGO/ZnO@ZBS-1; (b) spent RGO/ZnO@ZBS-1after 25 h reaction

3.4 Photocatalytic activity enhancement mechanism of RGO/ZnO@ZnS-Bi_2S_3

The enhanced photocatalytic activity over Bi_2S_3 containing composites is mainly related to the superior photo absorption in the visible region and the efficient generation, separation and transfer process of the photoinduced electron–hole pairs, which strongly depends on the band structure of the composites. Thus, the valence band (VB) edge positions and the conduction band (CB) edge positions of the RGO/ZnO@ZnS-Bi_2S_3 composite was estimated according to the following empirical formula:[27,13]

$$E_{VB}=X-E^e+0.5E_g \qquad (2)$$

$$E_{CB}=E_{VB}-E_g \qquad (3)$$

where E_{VB} is the VB edge potentials, E_{CB} is the CB edge potential, E_g is the band gap

energy of the semiconductor, X is the electronegativity of the semiconductor that is the geometric mean of the electronegativity of the constituent atoms, E^e is the energy of free electrons on the hydrogen scale (~4.5 eV). According to the X and E_g values (table 1), E_{VB} and E_{CB} of ZnO, ZnS and Bi_2S_3 were separately calculated as listed in table 1.

Table 1 the VB edge positions and CB edge positions of ZnO, ZnS and Bi_2S_3 estimated by empirical formula

Semiconductor	X/eV	E_g[a]/eV	E_{VB}/eV	E_{CB}/eV
ZnO	5.790	3.22[23,42,44]	2.90	-0.32
ZnS	5.265	3.43[13,44]	2.48	-0.95
Bi_2S_3	5.276	1.36[13,23,43]	1.45	0.09

[a] obtained from an average of E_g reported in cited literatures

Based on the reported work function of graphene (0.08eV vs. NHE)[45], E_{VB} and E_{CB} edge potentials of ZnO, ZnS and Bi_2S_3 calculated in table 1, the possible charge transfer process over RGO/ZnO@ZnS-Bi_2S_3 under irradiation of Xe lamp is proposed in Scheme 1. Clearly, Bi_2S_3 can be easily excited to form electron–hole pairs under visible light irradiation. Meanwhile, electrons in the VB of Bi_2S_3 could also be excited up to a higher potential edge (−0.95 eV) due to the higher photon energy. In the case of ZnS and ZnO, they cannot be excited by visible light irradiation with energy less than 2.95eV (420 nm) due to theirs wide energy gap. When Bi_2S_3 were introduced, the electrons in CB edge of Bi_2S_3 with potential more negative than that of ZnS (>−0.95 eV)[13] are produced, and these electrons on the Bi_2S_3 surface would easily transfer in sequence to ZnS, ZnO and RGO, leaving holes on the Bi_2S_3 valence band. Therefore, the photoinduced electrons and holes were separated efficiently. The electrons located on the RGO (-0.08 eV) can reduce H_2O to H_2 due to the higher potential than that of H_2/H^+. At the same time, the photoinduced holes at the VB top of Bi_2S_3 with potential of 1.45 eV which is more negative than the standard reduction potential of OH^-/OH (2.38 eV)[45] will directly oxidize glycerol to the final product CO_2. These well-separated photoelectrons and holes would explain the higher photocatalytic performance of Bi_2S_3-

containing composites compared to that of RGO/ZnO and RGO/ZnO@ZnS. However, with excess Bi_2S_3 content in the shell, more photoinduced electrons and holes would recombine easily on the surface of Bi_2S_3 due to the agglomeration of Bi_2S_3, and the decreasing in heterojunction amount between ZnS and Bi_2S_3, which reduces the photocatalytic activity of the RGO/ZnO@ZBS-3 composites.

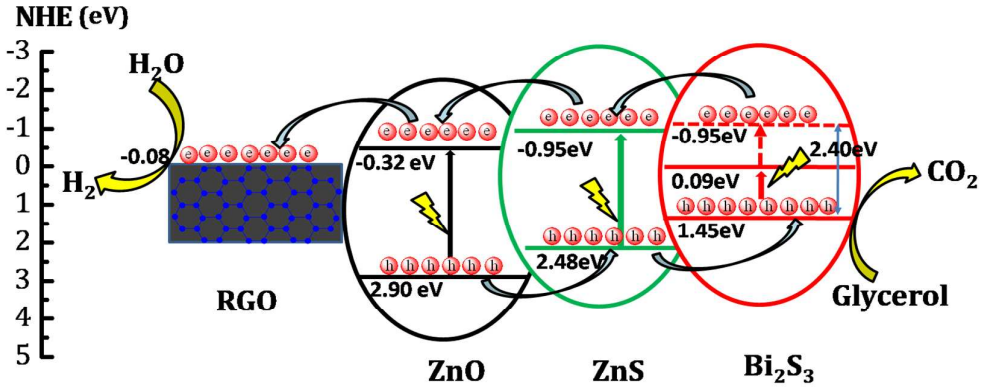

Scheme 1. A schematic diagram for the charge-transfer process in RGO/ZnO@ZnS-Bi_2S_3 nanocomposites

4 Conclusions

The nanocomposites of RGO/ZnO@ZnS-Bi_2S_3 with varying Bi_2S_3/ZnS molar ratios were successfully synthesized via combining the hydrothermal process and ion exchange technique. The as-prepared composite photocatalysts consist of core/shell nanorods with ZnO core and ZnS-Bi_2S_3 bi-component shell, which are anchored on the RGO sheets. These compostites exhibit enhanced photocatalytic activities in photocatalytic H_2 production from glycerol solution under the irradiation of Xe lamp. Under the optimal Bi_2S_3/ZnS molar ratio, the highest photocatalytic hydrogen production rate of 310μmol•h^{-1}•g^{-1} is observed. The highly improved performance of the composites can be ascribed to the increased light absorption and efficient charge separation. The facile approach presented in this study can be extended to the synthesis of other core/shell nanorods grown on RGO sheets with various functions.

Acknowledgement

We gratefully acknowledge the financial supports from the National Natural Science Foundation of China (No. 21276190 and 20806059).

Reference

1. M. R. Hoffmann, S. T. Martin, W. Choi, and D. W. Bahneman. *Chem. Rev.* 1995, **95**, 69-96.
2. H. X. Sang, X. T. Wang, C. C. Fan, F. Wang. *Int. J. Hydrogen Energy,* 2012, **37**, 1348-1355.
3. D. Lin, H. Wu, R. Zhang, W. Zhang, W. Pan, *J. Am. Ceram. Soc.,* 2010, **93**, 3384–3389.
4. Z. Wang, S. W. Cao, S. J. Loo and C. Xue, *CrystEngComm*, 2013, **15**, 5688–5693.
5. S. Sharma, S. Chawla, *Electron. Mater. Lett* ., 2013, **9**, 267-271.
6. W. Lia,G. Song, F. Xie, M. Chen, Y. Zhao, *Mater. Lett.,* 2013, **96** ,221–223.
7. F. Li, W. Bi, L. Liu, Z. Li, X. Huang, *Colloids Surf., A.* , 2009, **334** ,160–164.
8. S. Liu, X. T. Wang, W. Zhao, K. Wang, H. Sang, Z. He, *J. Alloys Compd.*, 2013, **568**, 84–91.
9. S. Liu, X. T. Wang, K. Wang, R. Lv, Y. L. Xu, *Appl. Surf. Sci.,* 2013, **283**, 732–739.
10. Y. F. Zhu, D. H. Fan, W. Z. Shen, *J. Phys. Chem. C,* 2008, **112**, 10402–10406.
11. R. Suarez, P. K. Nair, P. V. Kama, *Langmuir,* 1998, **14**, 3236-3241.
12. G. Konstantatos, L. Levina, J. Tang, E. H. Sargent, *Nano Lett.*, 2008, **8**, 4002-4006.
13. Z. Wu, L. Chen, C. Xing, D. Jiang, J. Xie, M. Chen, *Dalton Trans.*, 2013, **42**, 12980–12988
14. X. Liu, L. Pan, Q. Zhao, T. Lv, G. Zhu, T. Chen, T. Lu, Z. Sun, C. Sun, *Chem. Eng. J.,* 2012, **183**, 238–243.
15. Y. Zhang, Z. Chen, S. Liu, Y. Xu, *Appl. Catal., B*, 2013, **140–141**, 598–607.
16. S. Sarkar, D. Basak, *Chem. Phys. Lett.,* 2013, **561–562**,125–130.
17. T. Lv, L. Pan, X. Liu, T. Lu, G. Zhu, Z. Sun, *J. Alloys Compd*. ,2011, **509** , 10086–10091.
18. Q. P. Luo, X. Y. Yu, B. X. Lei, H. Y. Chen, D. B. Kuang, C. Y. Su, *J. Phys. Chem. C*, 2012, **116**, 8111−8117.
19. Y. Liu, Y. Hu, M. Zhou, H. Qian, X. Hu, *Appl. Catal., B*, 2012, **125**, 425–431.
20. D. Choi, M. Choi, W. Choi, H. Shin, H. Park, J. Seo, J. Park, S. Yoon, S. J. Chae, Y. H. Lee, S. W. Kim, J. Y. Choi, S. Y. Lee, J. M. Kim, *Adv. Mater.*, 2010, **22**, 2187–2192.
21. Y. Xiao , H. Cao, K. Liu, S.n Zhang , V. Chernow, *Nanotechnology,* 2010, **21**, 145601.
22. B. Li, T. Liu, Y. Wang, Z. Wang, *J. Colloid Interface Sci.*,2012, **337**, 114-221.
23. M. Ahmad, E. Ahmed, Z.L. Hong, J.F. Xu, N.R. Khalid, A. Elhissi, W. Ahmed, *Appl. Surf. Sci.,* 2013, **274**, 273-281.

24. G. Shen, D. Chen, C. J. Lee, *J. Phys. Chem. B,* 2006, **110**, 15689-15693.
25. Q. Xiong, J. Wang, O. Reese, L. C. Lew, Y. Voon, P. C. Eklund, *Nano Lett.*, 2004, **4**, 1991-1996.
26. Y. W. Koh, C. S. Lai, A. Y. Du, E. R. T. Tiekink, K. P. Loh, *Chem. Mater.*, 2003, **15**, 4544-4554.
27. J. Cao , B. Xu , H. Lin, B. Luo, S. Chen, *Dalton Trans.* , 2012, **41**, 11482-11490.
28. H. Fu, T. Xu, S. Zhu, Y. Zhu, *Environ. Sci. Technol.*, 2008, **42**, 8064–8069.
29. Q. Shou, J. Cheng, L. Zhang, B. J. Nelson, X. Zhang, *J. Solid State Chem.*, 2012, **182**, 191-197.
30. O. Akhavan, M. Mehrabian, K. Mirabbaszadeh, R .Azimirad, *J. Phys. D: Appl. Phys.,* 2009, **42**, 225-305.
31. H. Ma, J. Han, Y. Fu, Y. Song, C. Yu, X. Dong, *Appl. Catal., B*, 2011, **102**, 417–423.
32. S.Thirumaran , K. Ramalingam , G. Bocelli , A. Cantoni, *Polyhedron*,1999, **18**, 925–930.
33. Z. Fang,Y. Liu,Y. Fan, Y. Ni, X. Wei, K. Tang, J. Shen, Y. Chen, *J. Phys. Chem. C*, 2011, **115,** 13968–13976.
34. G. Singha , A. Choudhary, D. Haranath, A. G. Joshi, N. S., S. Singh, R. Pasrich, *Carbon*, 2012, **50**, 385– 394.
35. J.Q. Hu, Q. Li, X. M. Meng, C.S. Lee, S.T. Lee, *Chem Mater*, 2003, **15**, 305–308.
36. T. Wu, X. Zhou, H. Zhang, X. Zhong, *Nano Res* ,2010, **3**, 379–386.
37. V. M. Daskalaki, D. I. Kondarides, *Catalysis Today*, 2009, **144**, 75–80.
38. A. Patsoura, D.I. Kondarides, X. E. Verykios, *Appl. Catal. B*, 2006, **64**, 171–179.
39. A. Patsoura, D.I. Kondarides, X.E. Verykios, *Catal. Today*, 2007, **124**, 94–102.
40. D.I. Kondarides, V.M. Daskalaki, A. Patsoura, X.E. Verykios, *Catal. Lett.*, 2008, **122**, 26–32.
41. L. L. Qu, Z. J. Luo, C. Tang, Materials Research Bulletin, 2013, **48**, 4601–4605
42. S. Balachandran, M. Swaminathan. *Dalton Trans*., 2013, **42**, 5338-5347.
43. J. Cao, B. Xu, H. Lin, B. Luo, S. Chen. *Catal. Commun.*, 2012, **26**, 204–208 .
44. İ. Altına, İ. Polatb, E. Bacaksızb, M. Sökmena. *Appl. Surf. Sci.*, 2012, **258**, 4861–4865.
45. P. Gao, J. Liu, S. Lee, T. Zhang, D. D. Sun, *J. Mater. Chem.*, 2012, **22**, 2292-2298.
46. H. Røonneberg, G. Borch, R. Buchecker,N. Arpin, S. L. Jensen, *Phytochemistry*, 1982, **21**, 2087–2090.